Development of a universal nanobody-binding Fab module for fiducial-assisted cryo-EM studies of membrane proteins

Joël S. Bloch[a,1], Somnath Mukherjee[b,1], Julia Kowal[a], Ekaterina V. Filippova[b], Martina Niederer[a], Els Pardon[c], Jan Steyaert[c], Anthony A. Kossiakoff[b,d,2], and Kaspar P. Locher[a,2]

[a]Institute of Molecular Biology and Biophysics, ETH Zürich, 8093 Zürich, Switzerland; [b]Department of Biochemistry and Molecular Biology, University of Chicago, Chicago, IL 60637; [c]Structural Biology Brussels, Vrije Universiteit Brussel, B-1050 Brussels, Belgium; and [d]Institute for Biophysical Dynamics, University of Chicago, Chicago, IL 60637

Edited by Robert M. Stroud, University of California, San Francisco, CA, and approved October 13, 2021 (received for review August 21, 2021)

With conformation-specific nanobodies being used for a wide range of structural, biochemical, and cell biological applications, there is a demand for antigen-binding fragments (Fabs) that specifically and tightly bind these nanobodies without disturbing the nanobody–target protein interaction. Here, we describe the development of a synthetic Fab (termed NabFab) that binds the scaffold of an alpaca-derived nanobody with picomolar affinity. We demonstrate that upon complementary-determining region grafting onto this parent nanobody scaffold, nanobodies recognizing diverse target proteins and derived from llama or camel can cross-react with NabFab without loss of affinity. Using NabFab as a fiducial and size enhancer (50 kDa), we determined the high-resolution cryogenic electron microscopy (cryo-EM) structures of nanobody-bound VcNorM and ScaDMT, both small membrane proteins of ∼50 kDa. Using an additional anti-Fab nanobody further facilitated reliable initial three-dimensional structure determination from small cryo-EM test datasets. Given that NabFab is of synthetic origin, is humanized, and can be conveniently expressed in *Escherichia coli* in large amounts, it may be useful not only for structural biology but also for biomedical applications.

cryogenic electron microscopy | membrane protein | structure | antibody | nanobody

Antibodies have long been a cornerstone of cell biological and biochemical research because of their unique ability to bind with exquisite selectivity to an immense range of molecular targets. Engineering antibody fragments to introduce new functionalities is made possible by their modular form, which combines a conserved fold with a set of hypervariable loops (complementary-determining regions, CDRs) that confer the antibody's specificity and binding affinity. This conserved organization has guided endeavors to engineer novel forms and formats with enhanced properties to fabricate antibody-like molecules with increased functionality as research tools and biotherapeutic entities (1–7).

Antibodies have also been beneficial for structural biology. However, raising monoclonal antibodies using traditional hybridoma methodology has often constituted a significant barrier. In recent years, engineered antibody fragments have had a major impact on structural biology, particularly by accelerating the structure determination of membrane proteins. They were either applied as crystallization chaperones (8) or selected to trap specific states of a target protein, thereby reducing conformational flexibility (9). While the recent emergence of cryogenic electron microscopy (cryo-EM) has altered the structure determination landscape significantly, determining high-resolution structures of small particles (currently below ∼50 kDa) or highly dynamic macromolecules including membrane proteins remains challenging (10).

Two classes of antibody fragments have been widely and successfully used for structure determination: 1) fragment antigen binding (Fab) domains that consist of two protein chains and have an approximate molecular mass of ∼50 kDa and 2) heavy chain (HC)–only antibody fragments, also known as nanobodies (Nbs), which are found in camelids and sharks (5) and have an approximate molecular mass of ∼14 kDa. Unlike Fabs, Nbs are devoid of light chains (LCs), and the CDRs are located on a single Ig domain of the HC (VHH). Because of their groove- or cavity-binding propensity, Nbs can target epitopes that may be inaccessible to the larger Fabs. This has facilitated the trapping and stabilization of membrane proteins, such as transporters, ion channels, and receptors in distinct conformational states (11–15).

We and others have shown that Fab fragments are a game changer for cryo-EM studies of smaller proteins, particularly membrane proteins in which the surrounding detergent micelles or lipid nanodiscs impair the ability to align particles (16–21). While individually generating Fabs against membrane protein targets is possible, a more general approach using a universal fiducial would be desirable. In previous manifestations of universal fiducials, an "off-the-shelf" Fab was generated

Significance

Structural studies of membrane proteins by cryogenic electron microscopy (cryo-EM) often require antibody fragments (Fabs) to facilitate particle alignments and achieve high resolution. While conformational nanobodies have been developed to lock specific states of many membrane proteins, they only add 15 kDa of mass to the complex. We developed a synthetic Fab (NabFab) that rigidly binds the conserved scaffold of nanobodies, providing a universally applicable fiducial for cryo-EM studies of protein–nanobody complexes. We demonstrate the concept by determining two high-resolution structures of membrane proteins bound to specific nanobodies and NabFab. As the structural epitope for NabFab can be incorporated into the scaffold of virtually any nanobody, this raises the prospect of facile structure determination of many nanobody–protein complexes.

Author contributions: J.S.B., S.M., A.A.K., and K.P.L. designed research; J.S.B., S.M., J.K., E.V.F., M.N., and E.P. performed research; J.S. contributed new reagents/analytic tools; J.S.B., S.M., J.K., E.V.F., A.A.K., and K.P.L. analyzed data; and J.S.B., S.M., A.A.K., and K.P.L. wrote the paper.

The authors declare no competing interests.

This article is a PNAS Direct Submission.

[1]J.S.B. and S.M. contributed equally to this work.

[2]To whom correspondence may be addressed. Email: koss@bsd.uchicago.edu or locher@mol.biol.ethz.ch.

This article contains supporting information online at http://www.pnas.org/lookup/suppl/doi:10.1073/pnas.2115435118/-/DCSupplemental.

Published November 15, 2021.

to a binding motif that was introduced into the protein under investigation. For instance, we have designed and implemented universal Fab-based fiducials to BRIL (22, 23), to various classes of trimeric G proteins (24, 25), and to portable stem–loop RNA motifs (26). Additionally, a variety of other types of portable motifs have been developed (27, 28), some of which involve Nbs applied as the portable motif in a different context (29).

Given that many Nbs have been raised to trap or induce specific conformational states of target proteins, a universally applicable anti-Nb Fab would be beneficial. In this embodiment, the Nb provides the function, and the Fab provides the size and shape. We therefore pursued a strategy to develop a "universal" fiducial that combines the attributes of both the Nb and Fab fragments into one unit. We describe here the development and implementation of a universal anti-Nb Fab (NabFab) that can be readily applied to almost any Nb–protein complex. NabFab has been engineered to attach distal to the Nb's CDR loops and at an angle that ensures that it does not interfere with the Nb's target. We show how the NabFab is compatible with virtually all Nb scaffolds, enabling easy "plug and play" use. We demonstrate the utility of NabFab by determining high-resolution cryo-EM structures of two distinct ∼50-kDa membrane proteins. Capitalizing on the humanized scaffold (30, 31) of the NabFab, we employed a second Nb that binds to the hinge connecting the variable and constant domains of the NabFab LC (32). This adds a distinct feature that breaks the pseudosymmetry of the Fab to facilitate the analysis of three-dimensional reconstructions in small cryo-EM test datasets. With these findings, we demonstrate the applicability of NabFab as a powerful fiducial for cryo-EM, thereby enabling the structure determination of many important biological systems that have existing Nb binders available to them. To facilitate broad use of NabFab, the expression plasmid and associated protocols are freely available upon request.

Results and Discussion

Generation and Characterization of a Synthetic Anti-Nb Fab (NabFab). The workflow for developing, validating, and utilizing a universal Nb–Fab system is outlined in Fig. 1*A*. In the first step, a cohort of anti-Nb Fabs was generated by phage display mutagenesis utilizing a high-diversity ($\sim 10^{10}$), synthetic phage display library based on a humanized antibody Fab scaffold (30). The target antigen was an alpaca-derived Nb (TC-Nb4) against the complex of human transcobalamin and its cognate receptor TCblR/CD320 (33). To obtain Fabs that bind an epitope distal to the CDRs of TC-Nb4, the selection was performed in the presence of molar excess of its cognate target TC:CD320 (34), which effectively masked the CDR loops. After four rounds of selection, the enrichment of specific binders over nonspecific background clones was >50-fold. DNA sequencing of clones that gave a strong signal over background in single point phage enzyme-linked immunosorbent assay (ELISA) resulted in 12 unique binders. The high diversity in CDR-H3 and L3 indicated that the cohort of clones represented a large diverse pool. These binders were subcloned into Fab format for expression in *Escherichia coli.* Out of 12, 11 Fabs were successfully expressed and purified in large scale.

While Nbs have a common structural scaffold, their surface residues are not fully conserved. We anticipated that the Fabs selected against TC-Nb4 might bind an epitope that was not fully compatible with all possible Nb scaffold sequences. We therefore adopted a grafting strategy to ensure the binding of other Nbs, no matter their sequence variation or CDR loop composition, to the Fab selected against TC-Nb4. The CDR loops from target Nbs could likely be inserted in the scaffold of

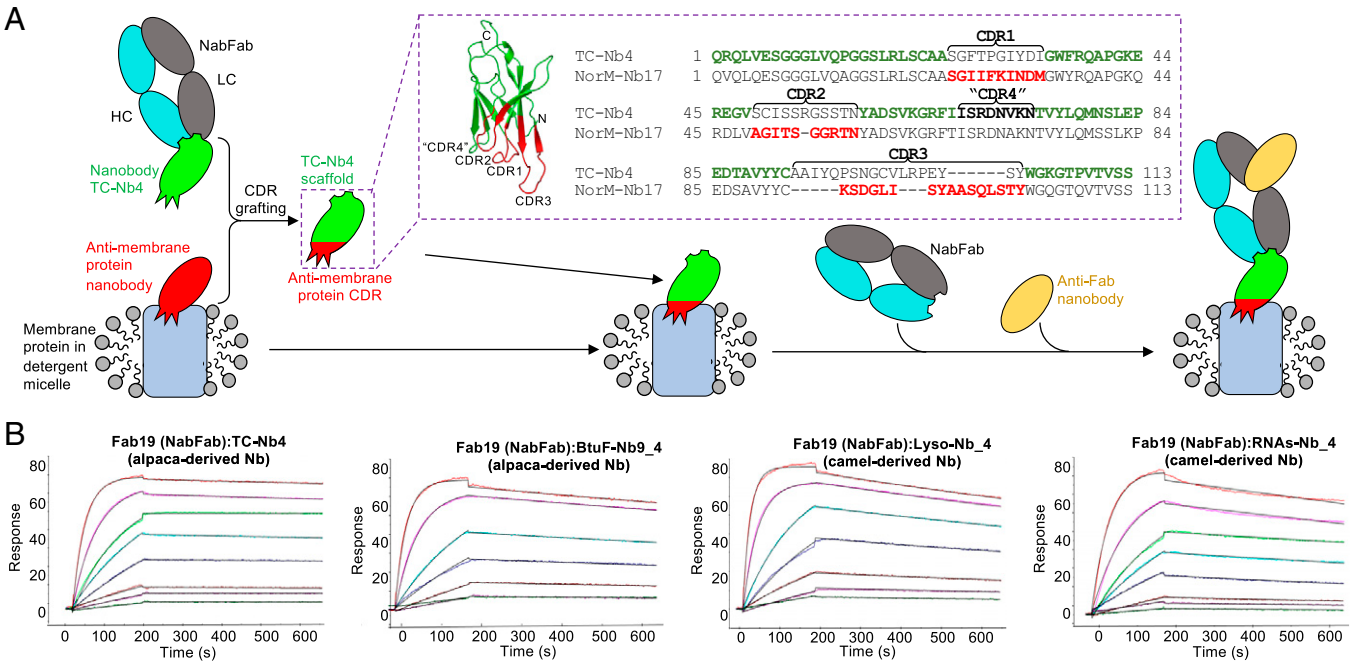

Fig. 1. Universal binding of NabFab to the scaffold Nbs enabled by CDR grafting. (*A*) Schematic of NabFab application in Nb binding. The grafting of target-specific Nb CDRs onto the TC-Nb4 (33) scaffold, which contains the NabFab-binding epitope, enables rigid complex formation of target membrane protein, grafted Nb, NabFab, as well as an anti-Fab Nb (32) as symmetry breaker. Dashed boxes illustrate the rationale behind CDR grafting. On the example of the structure of NorM-Nb17_4 (ribbon representation), the TC-Nb4 scaffold (33) is shown in green and the grafted CDRs of NorM-Nb17 in red. On the right side, a sequence alignment of TC-Nb4 and NorM-Nb17 is shown in Kabat numbering (48). The scaffold and CDR regions that comprise the grafted NorM-Nb17_4 are highlighted with the same colors. Note that for NorM-Nb17_4, "CDR4" of TC-Nb4 was retained due to its similarity in sequence. (*B*) SPR sensograms of NabFab binding to TC-Nb4 (alpaca) and grafted Nbs BtuF-Nb9_4 (alpaca), Lyso-Nb_4 (camel), and RNAs-Nb_4 (camel).

TC-Nb4 to obtain chimeras that retain the binding properties of the original Nb. Conceptually, this is the same process involved in the "humanization" of antibodies. We tested the feasibility of the approach using Nbs of distinct origin by swapping their CDR loops into the scaffold of TC-Nb4 guided by the sequence boundaries shown in Fig. 1*A*. We used Nbs targeting the vitamin B_{12}–binding bacterial protein BtuF (35), lysozyme (36), and RNAseA (37), resulting in the chimeras BtuF-Nb9_4, Lyso-Nb_4, and RNAs-Nb_4. Analytical size-exclusion chromatography (SEC) combined with gel electrophoresis experiments (*SI Appendix*, Fig. S2) demonstrated that the chimeric Nbs bound their cognate antigen targets, indicating the robust nature of the engineered scaffold. Next, the cross-reactivity of the 11 generated Fabs to the three Nb chimeras was tested by a single-point protein ELISA experiment (*SI Appendix*, Fig. S1). While all Fabs bound to the parent TC-Nb4 scaffold, several showed little or no cross-reactivity to the Nb chimeras. We speculate that the binding of these Fabs may be affected by the antigen used in the selection, demonstrating the importance of experimentally confirming that the Fabs to be carried forward are devoid of antigen influence. Fab14 and Fab19 displayed strong binding to all four chimeric Nb constructs, and the binding affinity and kinetics to TC-Nb4 were measured by surface plasmon resonance (SPR). Fab19 and Fab14 bind to TC-Nb4 with affinities (K_D) of 860 pM and 21 nM, respectively (Table 1). While both Fab14 and Fab19 are high-affinity binders for most structural biology applications, Fab19 is superior because it has an ∼60-fold slower off-rate than Fab14. We evaluated the binding of Fab19 to the other three chimeric Nbs, demonstrating that it bound all three with low-nanomolar affinity (Table 1 and Fig. 1*B*).

We next evaluated how Fab19 would perform in the context of Nbs binding to membrane proteins. We selected three Nbs targeting the bacterial MATE transporter VcNorM (llama-derived NorM-Nb17_4), the bacterial divalent metal ion transporter ScaDMT (38) (llama-derived DMT-Nb16_4), and the bacterial oligosaccharyltransferase PglB (39) (alpaca-derived PglB-Nb17_4). As in the case with the soluble targets, SEC analysis demonstrated that Fab19 binds to the chimeric Nbs in the context of their cognate membrane protein targets (*SI Appendix*, Fig. S2). Thus, based on Fab19's high affinity, superior kinetic profile, and its performance with chimeric Nbs derived from different species and targeting both soluble and membrane protein systems, it was designated as the lead candidate (NabFab) to be further tested as a universal Nb fiducial in a series of cryo-EM experiments.

Fiducial-Assisted, Single-Particle Cryo-EM Structure Determination. To assess the potential of NabFab as a fiducial to enhance size and shape to assist in the alignment of small particles for cryo-EM structure determination, we chose two ∼50 kDa–sized membrane proteins, VcNorM and ScaDMT. These membrane proteins have no significant extramembranous features and are of a size that is representative of many important biotherapeutic targets and remain challenging targets for cryo-EM. While the X-ray structure of VcNorM has been reported without bound Nbs (40), that of ScaDMT had been determined in complex with a llama-derived Nb (DMT-Nb16) (38). For VcNorM, we generated a specific Nb by immunization of llama (41). For the use with NabFab, we generated the chimeric Nbs NorM-Nb17_4 and DMT-Nb16_4.

Table 1. Kinetic parameters of Fabs binding to wt TC-Nb4 and scaffold-grafted Nbs

Fab	Nb	k_{on} ($M^{-1} \cdot s^{-1}$)	k_{off} (s^{-1})	K_D (nM)
Fab14	TC-Nb4	4.2×10^5	8.8×10^{-3}	21
NabFab (Fab19)	TC-Nb4	1.6×10^5	1.4×10^{-4}	0.9
	BtuF-Nb9_4	1.1×10^5	4.2×10^{-4}	3.9
	Lyso-Nb_4	2.2×10^5	3.5×10^{-4}	1.6
	RNAs-Nb_4	1.8×10^6	3.0×10^{-4}	1.7

VcNorM and ScaDMT were purified in detergent (dodecyl maltoside, DDM) and incubated with the grafted chimeric Nbs, NabFab, and an anti-Fab Nb that had been raised to bind to the elbow linker between the variable and constant domains of the Fab's LC (31). In our previous work, we found this anti-Fab Nb markedly improved the attributes of the Fab fiducials. First, it reduces the inherent flexibility between the variable and constant domains, which is Fab dependent (42). Second, even though the size of the elbow Nb only marginally increases the mass of the NabFab, it adds a distinctive element to the shape of the fiducial that assists in particle alignment. Combining the four components yielded stochiometric complexes (*SI Appendix*, Fig. S2) that were directly applied to cryo-EM grids and subjected to cryo-EM analysis (Fig. 2). Note that NabFab does not bind the scaffold of the anti-Fab Nb, which prevents Fab–Nb polymerization.

The distinct structural features of the complexes were readily visible in the motion-corrected micrographs (Fig. 2 *A* and *E*) and became more evident during two-dimensional (2D) classification (Fig. 2 *B* and *F*). We were able to determine initial models from sets of particles obtained from 380 (VcNorM) or 625 (ScaDMT) micrographs that were collected in under 2 h at a Titan Krios cryo-transmission electron microscope. For each complex, a reconstruction could be refined to ∼12 Å resolution, using as few as ∼10,000 particles (Fig. 2 *C* and *G*). At this stage of analysis, two features of the fiducial were readily apparent. First, there was a discernable hole between the variable and constant domains of NabFab, which is a hallmark of all Fab fiducials. Second, the anti-Fab Nb provided a distinct feature that allowed the handedness of the obtained reconstruction to be correctly assigned even at low resolution given the characteristic shape of the NabFab:anti-Fab Nb complex (32). This is advantageous for rapid analysis of small cryo-EM test datasets using NabFab.

Upon collecting larger datasets, we obtained three-dimensional (3D) reconstructions at final resolutions of 3.47 Å for VcNorM and 3.78 Å for ScaDMT (Fig. 2 *D* and *H*, *SI Appendix*, Figs. S3 and S4 and Table S1). In both structures, a rigid NabFab–Nb interface was observed (*SI Appendix*, Figs. S5 and S6). Local resolution estimates indicate that differences in the flexibility of the two membrane proteins might have led to the observed resolution differences. The higher rigidity of VcNorM compared with ScaDMT can probably be attributed to the bound Nb NorM-Nb17_4, whose CDRs are deeply wedged into the outward-open cavity of the transporter. In the VcNorM structure, we increased the local resolution of different regions of the complex by shifting of the map fulcrum (*SI Appendix*, Fig. S5), which was originally placed at the center of the membrane protein by the processing software RELION3.1 (43). VcNorM was in a similar outward-facing state as in previously published structures (40). However, the improved resolution allowed us to build a de novo model, which revealed that significant registry errors exist in the published structure. A detailed analysis of the cryo-EM structure of VcNorM will be published elsewhere.

For ScaDMT, our electron microscopy (EM) map was of similar quality as that of the previously published X-ray structures (38). A notable difference we observed was the dimerization state of ScaDMT with DMT-Nb16. While the original DMT-binding Nb promotes dimerization of the DMT-Nb complex in solution and in the crystal lattice (38), the chimeric DMT-Nb16_4 does not allow a similar association of DMT-Nb complexes. We therefore observed mainly monomeric complexes of DMT and no Nb-mediated dimerization. However, we identified a subclass of ScaDMT-Nb complex dimers (*SI*

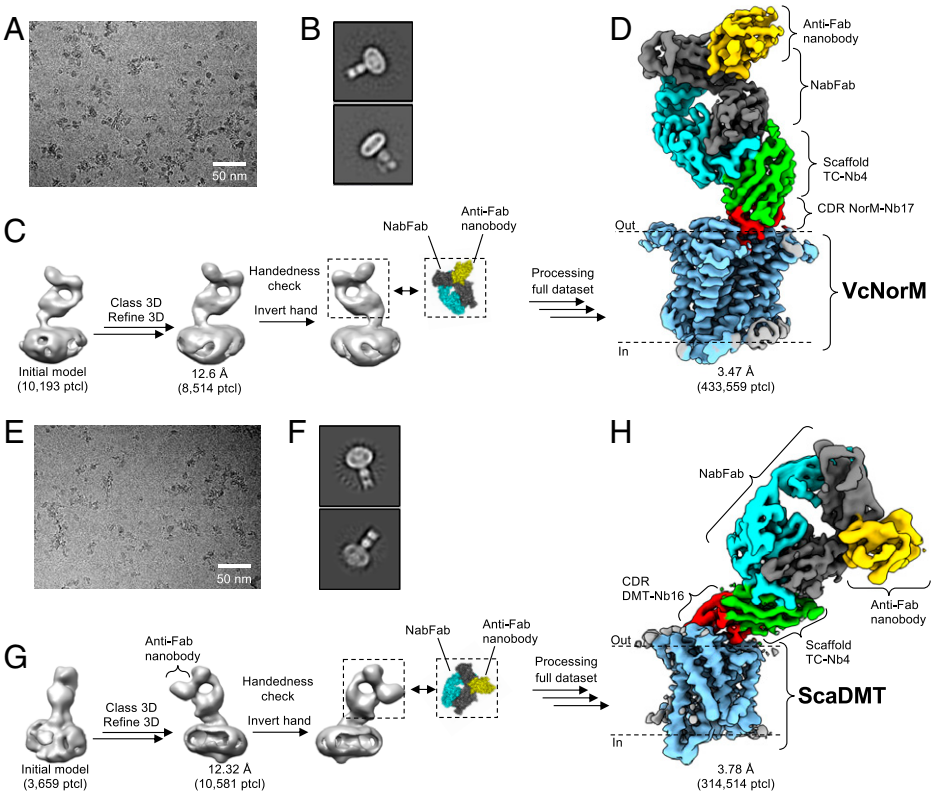

Fig. 2. Fiducial-assisted structure determination. (*A–D*) Cryo-EM structure determination of VcNorM complex. (*E–H*) Cryo-EM structure determination of ScaDMT complex. (*A* and *E*) Representative cryo-EM micrographs of complexes of detergent-solubilized membrane protein, grafted Nb, NabFab, and anti-Fab Nb. (*B* and *F*) Representative 2D classes as calculated in RELION 3.1 (43). (*C* and *G*) Processing of a small cryo-EM test dataset including initial model generation and 3D refinement as calculated in RELION 3.1 (43) and assignment of the correct handedness of the structure using structural knowledge of NabFab:anti-Fab Nb complex. (*D* and *H*) Unsharpened cryo-EM maps of VcNorM and ScaDMT complexes derived from the processing of full datasets [VcNorM in RELION 3.1 and ScaDMT in RELION 3.1 (43) and cryoSPARC V3.2 (49)]. VcNorM and ScaDMT are highlighted in light blue, grafted Nb CDRs in red, TCNb4 scaffold in green, NabFab HC in cyan and LC in black, and the anti-Fab Nb in yellow.

Appendix, Fig. S4 *B* and *F*) with an arrangement distinct from the published structure (38). Although the resolution of this dimeric reconstruction was low (~8.5 Å), the chiral NabFab: anti-Fab Nb handle allowed us to unambiguously fit ScaDMT into the EM density. The observed dimer interface is formed by TM7 and EL3-H1 of ScaDMT and does not appear to be caused or influenced by any of the involved Fabs or Nbs. This finding may reflect a mode of homodimerization for ScaDMT or other SLC11/NRAMP family members.

Fab–Nb Interface. In addition to the two cryo-EM structures, we also determined a 3.2-Å crystal structure of NabFab in complex with Lyso-Nb_4 (*SI Appendix*, Table S2) and compared it with the cryo-EM structures containing VcNorM and ScaDMT. While the three complexes each contained a single copy of NabFab and a bound Nb, the CDRs of the Nbs are distinct. Remarkably, the three NabFab–Nb interfaces (Fig. 3 *A–D*) are indistinguishable at the present resolution, demonstrating the effectiveness of our CDR-grafting strategy. An interface analysis revealed the conserved interactions among the three structures (*SI Appendix*, Table S3). The two EM maps and the X-ray map are well resolved at the NabFab–Nb interface and even revealed bound water molecules, most of which are visible in all three structures (Fig. 3 *E–G*). This underscores the structural rigidity of the interface, which is an important factor to consider in determining the potential of a fiducial mark.

NabFab binds the β-strands of the TC-Nb4 scaffold mostly via its long CDR3 loop of the HC. Additional contacts are provided by the CDR1 of the HC and by the CDR2 of the LC. The C-terminal His-tags of the NorM-Nb17_4 and DMT-Nb16_4 Nbs are partially ordered in the EM density maps and appear to weakly interact with the LC scaffold but, given the absence of a His-tag in the purified Lyso-Nb_4 molecule, these contacts are likely not essential. The buried surface area between NabFab and the Nb scaffold amounts to an average of 976 $Å^2$ (731 ± 23 $Å^2$ for the HC and 245 ± 18 $Å^2$ for the LC). There are several prominent π–π and cation–π interactions involving aromatic NabFab residues (Fig. 4*A*). To identify the hotspot residues that must be retained during scaffold grafting, we generated alanine mutants of the interface residues of the CDR-grafted LysoNb_4 Nb and tested their respective affinities to NabFab by SPR (Fig. 4*B*, *SI Appendix*, Table S4). The most significant reduction in affinity was observed for P41 and V89 in which mutations to alanine reduced the affinity between 400- to 600-fold, resulting in $\Delta\Delta G°$ values of 3.6 and 3.8 kcal · mol^{-1}, respectively (Figs. 4*B* and 5*A*). Substantial effects were also observed upon mutation of R45 (>40-fold higher K_D) and Y91 (>25-fold higher K_D), whereas mutating L11, K43, W103, or S112 to alanine only marginally (<fivefold) reduced the affinity of NabFab to LysoNb_4. Notably, our alignments suggest that NabFab binding extends beyond camelid-derived Nbs. Based on sequence alignments, our grafting strategy appears to be compatible with the scaffolds used in the synthetic Nb libraries NbLib (44) and Sybody (45) with relatively few changes (*SI Appendix*, Fig. S7).

Structural Considerations for a Universal Anti-Nb Fab. As part of the phage display selection process, we employed an epitope-

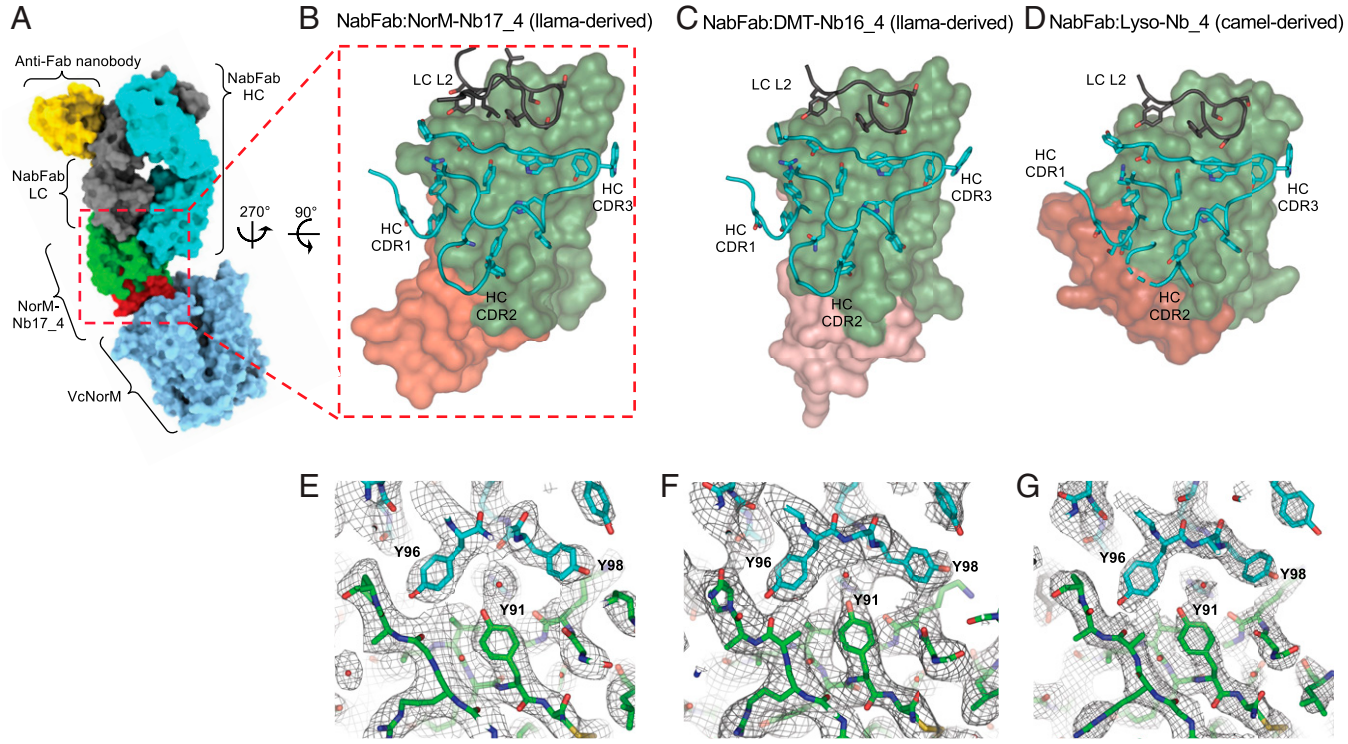

Fig. 3. Structural analysis of NabFab binding to grafted Nbs of different origin. (*A*) Surface representation of complex of VcNorM (blue), NorM-Nb17_4 TC-Nb4 (33) scaffold green, NorM-Nb17 CDRs red), NabFab (HC cyan, LC black), and anti-Fab Nb (32) (yellow). (*B*) Zoomed-in view of NorM-Nb17_4:NabFab-binding interface with NorM-Nb17_4 in surface representation and NabFab in ribbon representation with interface residues in stick representation with oxygen atoms colored in red and nitrogen atoms in blue. (*C*) DMT-Nb17_4:NabFab-binding interface. (*D*) Lyso-Nb_4:NabFab-binding interface. (*E*) Representative section of EM map of NorM-Nb17_4:NabFab interface at 12 rmsd, carved to 2 Å. Ordered water molecules indicated by red crosses. (*F*) Representative section of EM map of DMT-Nb16_4:NabFab interface at 11 rmsd, carved to 2 Å. (*G*) Representative section of electron density of Lyso-Nb_4:NabFab interface at 1 rmsd, carved to 2 Å.

masking strategy to focus the available binding epitopes on the distal side of the Nb relative to the CDR loops. However, while the epitope location is important, it is the orientation of the Fab extending from the epitope that is of most consequence. The relative angles defined by the orientation of the Fab to the Nb and the Nb to its membrane target combine to delineate the potential universality of the Fab. NabFab engages the TC-Nb4 scaffold at an obtuse angle with respect to the centroid of the CDR residues, orienting it away from the antigen target. Another important factor is the angle of engagement of the Nb to its target. In the examples described here, the chimeric Nbs for VcNorM and ScaDMT

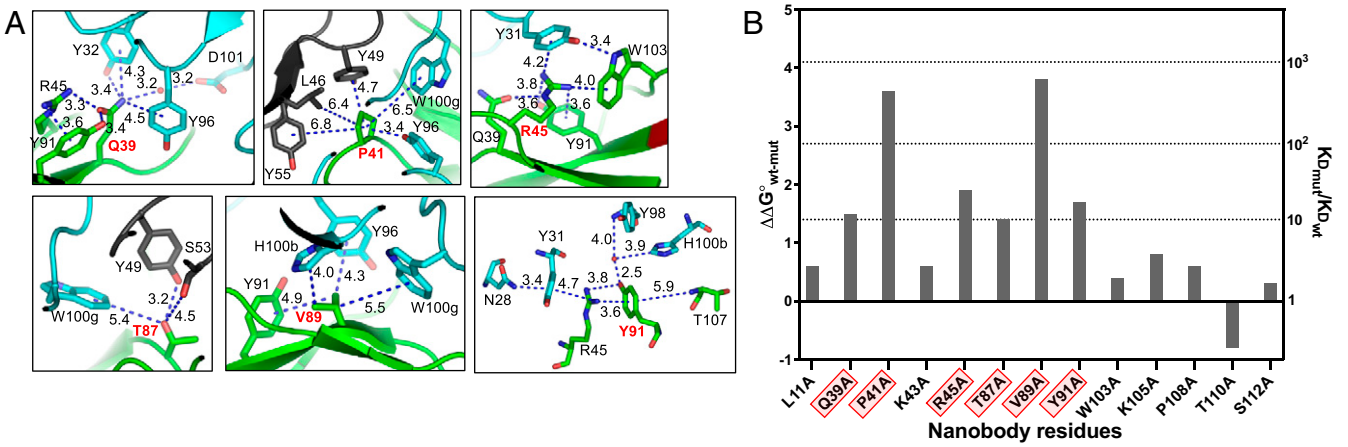

Fig. 4. Hotspot analysis of NabFab-binding epitope on TC-Nb4 scaffold. (*A*) Detailed views of NorM-Nb17_4 residues at the NabFab-binding interface. Distances in angstrom are indicated with numbers and dotted lines. Note that R45 and Y91 are contributing to a cation–π ladder. (*B*) Alanine scanning of Nb residues at the interface to NabFab. Bars indicate the ratio of the K_D for NabFab binding to the original TC-Nb4 scaffold and the respective surface mutants as derived from SPR measurements. Residues for which mutation to Ala reduced binding affinity more than 10-fold are highlighted in red. Note that Lyso-Nb_4 was used in this experiment.

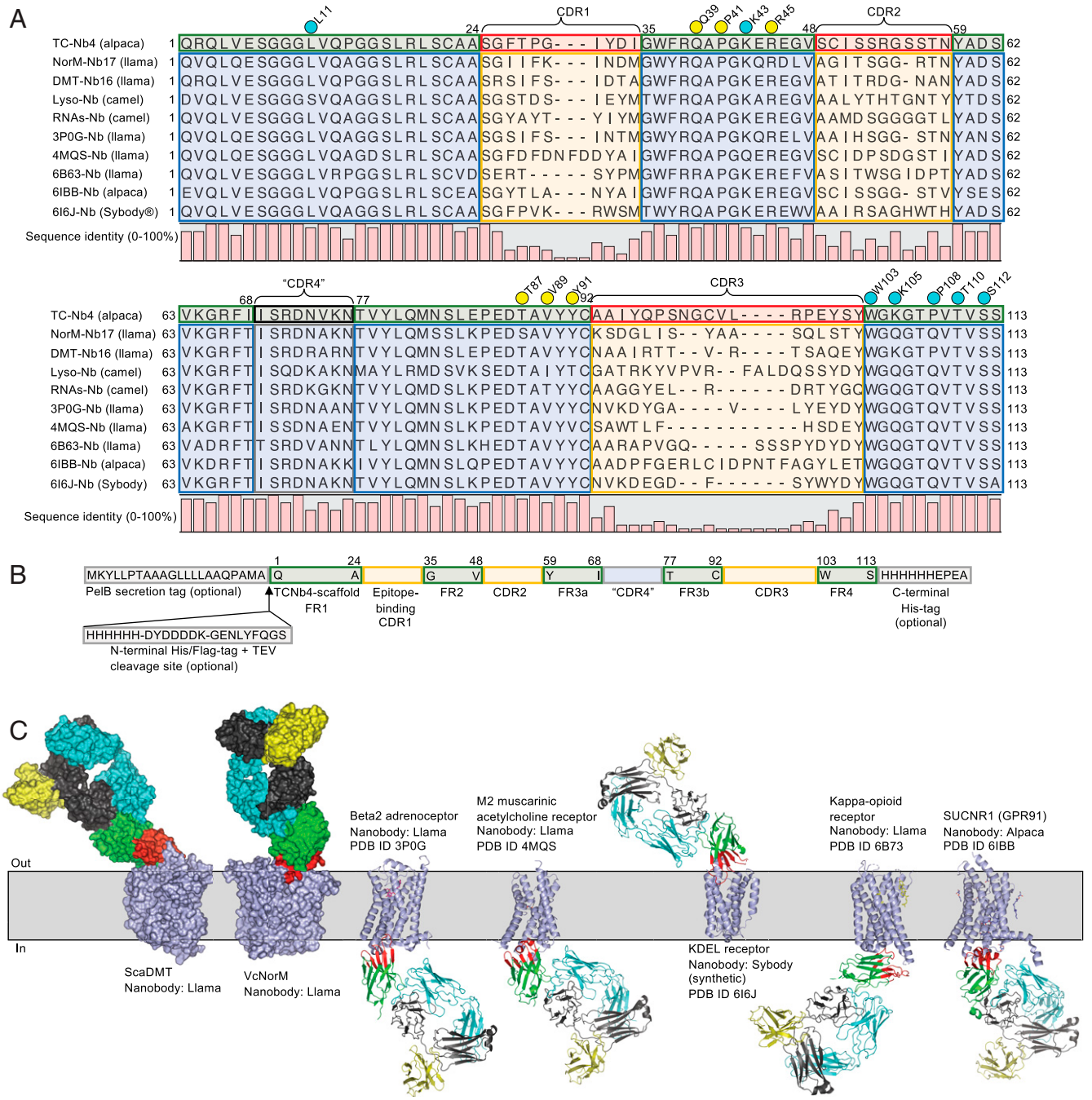

Fig. 5. In silico CDR grafting and NabFab-binding analysis for potential structural targets. (*A*) Protein sequence alignment of TC-Nb4 (33), NorM-Nb17, DMT-Nb16 (38), and Lyso-Nb (36), as well as selected Nbs of known membrane protein–Nb complexes (11–13, 50, 51) (PDB IDs: 3P0G, 4MQS, 6B73, 6IBB, and 6I6J), generated with Clustal Omega (52), in Kabat numbering (48). Green boxes indicate scaffold regions of TC-Nb4. Blue boxes indicate equivalent scaffold regions other Nbs. Red boxes indicate CDRs of TC-Nb4. Yellow boxes indicated equivalent CDR regions of other Nbs. A black box indicates "CDR4" of TC-Nb4. A gray box indicates the equivalent region in other Nbs. Note that "CDR4" is a nonvariable loop that in some cases interacts with the target protein of the respective Nb. Residues at the Nb-binding interface to NabFab are indicated with colored dots on top. Yellow dots indicate a strong contribution to NabFab binding. Cyan-colored dots indicate a weak contribution, as described in Fig. 3*B*. (*B*) Schematic of CDR-grafting strategy: Green boxes indicate regions of the TC-Nb4 scaffold that were retained during grafting. Yellow boxes indicate epitope-binding CDR regions of different Nbs that were grafted into the TC-Nb4 scaffold. A gray/blue box indicates "CDR4," which can also be grafted. Flanking gray boxes indicate the secretion and purification tags. Note that the His-tags are not necessary for NabFab binding. (*C*) Structures of complexes of VcNorM and ScaDMT in surface representation as well as selected examples of in silico docked [PyMol (53)], putative complexes of selected membrane protein–Nb complexes in ribbon representation. Membrane proteins are colored in blue, original Nb CDRs in red, TC-Nb4-scaffold in green, NabFab HC in cyan, NabFab LC in gray, and anti-Fab Nb in yellow.

bind to their respective targets at significantly different angles, yet the bound NabFab pointed away from the detergent micelle and proved to be an effective fiducial in both cases (Fig. 2).

To explore the applicability of NabFab, we performed an in silico analysis of 31 structures of integral membrane proteins smaller than 100 kDa, bound to a Nb, and available in the Research Collaboratory for Structural Bioinformatics (RCSB)

Protein Data Bank (PDB). We superimposed our NabFab: NorM-Nb17_4 complex onto the Nb entities in these structures. We found that in 84% of the cases, NabFab neither clashes with the target protein nor with the lipid bilayer (*SI Appendix*, Table S5). We then generated structure-based sequence alignments of five representative examples (Fig. 5*A*). These alignments establish the precise boundaries within the Nb scaffold and suggest a CDR-grafting protocol (Fig. 5*B*) that will ensure that the chimeric Nbs retain specificity for a given target proteins while binding NabFab with maximum affinity. In addition to the hypervariable CDR loops (CDR1, CDR2, and CDR3), we advise to also graft a fourth loop, referred to as "CDR4," because this loop is not 100% conserved in Nbs and occasionally contributes to the binding of target proteins. Notably, as neither of the Nb termini is involved in NabFab binding, the location of a purification tag of the chimeric Nb construct can be chosen freely. Thus, our analysis suggests that NabFab will likely be applicable for cryo-EM studies of a wide range of integral membrane protein–Nb complexes, including solute carriers and G protein–coupled receptors (selected examples shown in Fig. 5*C*).

Conclusions

We have developed and validated a universal cryo-EM fiducial for the study of protein–Nb complexes. It is a robust and reliable tool based on its ability to strongly and specifically bind the engineered scaffold portion of folded Nbs. We provide an easy-to-follow grafting strategy that facilitates the repurposing of Nb scaffolds to ensure binding to the universal Fab (NabFab), irrespective of the origin of the Nb. NabFab is conveniently expressed in *E. coli*, and its synthetic nature allows it to be further engineered to introduce other labels that could be useful for complementary cell biology studies or to facilitate other binding proteins. Our results suggest that NabFab is not only useful for high-resolution structure determination of small (membrane) proteins by cryo-EM, but its shape characteristics with the attached anti-Fab elbow Nb can be powerfully exploited for the rapid assessment of test datasets.

Despite recent advances in the prediction of 3D structures by artificial intelligence–based algorithms (46, 47), determining experimental high-resolution structures of proteins in distinct conformational states and bound to ligands and inhibitors remains essential for basic science and drug development. Many researchers have generated Nbs against membrane proteins, often trapping specific functional states. NabFab offers a convenient way for those projects to transition from X-ray to cryo-EM or to increase the resolution of cryo-EM studies. NabFab binding also appears compatible with the simultaneous application of megabodies (29), which might help to improve particle solubility and orientational distribution.

Finally, NabFab might be useful for other applications: the rigid linkage of NabFab to target Nbs might improve the precision of single-molecule imaging studies using Förster resonance energy transfer. Moreover, the humanized scaffold of NabFab combined with the low immunogenicity of Nbs (6) also offers opportunities in medical imaging or drug development.

Methods

Expression and Purification of Nbs. TC-Nb4, NorM-Nb17_4, DMT-Nb17_4, PglB-Nb17_4, and TC-Nb11_4 were purified as described previously (33).

BtuF-Nb9_4, Lyso-Nb_4, and RNAs-Nb_4 were cloned into the vector pET26b+, resulting in N-terminally His-tagged fusions. These were expressed in *E. coli* C43(DE3) in Terrific Broth media supplemented with 0.4% (vol/vol) glycerol. Cells were grown until mid-log phase at 37 °C, induced with 1 mM IPTG, and grown for 16 to 20 h at 25 °C. Nbs were purified by Ni-NTA chromatography followed by SEC using Superdex75 increase columns. For crystallization trials with the Lyso-Nb_4, the His-tag was cleaved with tobacco etch virus (TEV) protease followed by a subtractive Ni-NTA chromatography before SEC experiments.

Enzymatic Biotinylation of Nbs. Nbs were biotinylated via C-terminal insertion of the amino acid sequence `(GGGS)3-GLNDIFEAQKIEWHE-GGGS-H6` and subsequent BirA-mediated biotinylation, as described previously (34). The extent of labeling was verified by a streptavidin (SA) pull-down assay.

Grafting of CDRs into Nb TCNb4 Scaffold. Based on structural comparisons and sequence alignments in Clustal Omega (52) of different Nbs, a grafting strategy was implemented as outlined in Fig. 5*B*. For expression in *E. coli*, Nbs were fused to an N-terminal PelB secretion sequence (MKYLLPTAAAGLLLLAAQPAMA-Nanobody), which is naturally cleaved during bacterial expression. According to Kabat numbering (48), residues 1 to 24, 35 to 48, 59 to 68, 77 to 92, and 103 to 113 of TC-Nb4 were combined with the respective CDRs of the Nb of interest. For NorM-Nb17_4, "CDR4" of TC-Nb4 was retained, as it was very similar to that of NorM-Nb17. For purification, either 1) an N-terminal His_6-Flag-TEV cleavage site (PelB-HHHHHH-SSDYKDDDDK-GENLYFQGS-Nanobody) was inserted or 2) a C-terminal His_6-CaptureSelect C-tagXL (PelB-Nanobody-HHHHHH-EPEA) was used. Strategy one was used for ButF-Nb9_4, Lyso-Nb_4, and RNAs-Nb9_4 and option two for TC-Nb4, NorM-Nb17_4, DMT-Nb17_4, and PglB-Nb17_4.

Phage Display. The selection for the TC-Nb4 target was performed as follows: In the first round of the selection, 200 nM of the target was immobilized on SA magnetic beads followed by washing to remove unbound protein and an incubation with D-biotin to block unoccupied SA sites on the beads. The beads were then incubated with the phage library (30), containing 10^{12} to 10^{13} virions/mL for 30 min at room temperature. The resuspended beads containing bound phages after extensive washing were used to infect freshly grown log phase *E. coli* XL1-Blue cells. Phages were amplified overnight in 2× yeast tryptone media with 50 μg/mL ampicillin and 10^9 plaque-forming units/mL of M13 KO7 helper phage. Three additional rounds of sorting were performed with decreasing target concentration in each round (second round: 100 nM, third round: 50 nM, and fourth round: 10 nM) using the amplified pool of virions of the preceding round as the input in a semiautomated platform using the Kingfisher instrument. From the second round onwards, 5 μM TC:CD320 were used in all the binding and washing steps to prevent the phage pool from binding to the CDRs of TC-Nb4. Also, from the second round onward, bound phages were eluted using 0.1 M glycine, pH 2.7. This technique often risks the enrichment of nonspecific and SA binders. Thus, the precipitated phage pool was negatively selected against SA beads before each round. The "precleared" phage pool was then used as an input for the next round in the campaign. Colonies from the fourth round of selection were subjected to phage ELISA according to published protocols (21).

Protein ELISA. Protein-based single-point ELISA was performed to determine the cross-reactivity of the Fabs to the different Nbs in the grafted TC-Nb4 scaffold. A total of 50 nM each of TC-Nb4, BtuF-Nb9_4, Lyso-Nb_4, and RNAs-Nb_4 were immobilized on ELISA plates followed by incubation with 250 nM purified Fabs 1, 2, 6, 12, 14, 16, 18, 19, 21, 23, and 28. The plates were washed, and the bound antigen-sAB complexes were incubated with a secondary horseradish peroxidase–conjugated protein L (1:5,000 dilution in phosphate-buffered saline containing 0.05% [vol/vol] Tween-20). The plates were washed, developed with 3,3′,5,5′-tetramethylbenzidine substrate, and quenched with 1.0 M HCl, and absorbance (A_{450}) was determined.

Cloning, Overexpression, and Purification of Fabs. *E. coli* C43 (DE3) Pro+ cells were transformed with Fabs cloned in the expression vector pRH2.2 (54). Cells were grown in Terrific Broth autoinduction media with 100 μg/mL ampicillin at 25 °C for 16 h. Harvested pellets were resuspended in phosphate-buffered saline supplemented with 1 mM PMSF and 1 μg/mL deoxyribonuclease I. The suspension was lysed by ultrasonication. The cell lysate was incubated at 65 °C for 30 min. Heat-treated lysate was then cleared by centrifugation, filtered through a 0.22-μm filter, and loaded onto a 5-mL HiTrap protein L column pre-equilibrated with 20 mM Tris pH 7.5, 500 mM NaCl. The column was washed extensively with 20 mM Tris pH 7.5, 500 mM NaCl followed by an elution of Fabs with 0.1 M acetic acid. The eluted protein was directly loaded onto a 1-mL ResourceS column pre-equilibrated with 50 mM NaOAc pH 5.0. The column was washed with the equilibration buffer, and Fabs were eluted with a linear gradient 0 to 50% of 50 mM NaOAc pH 5.0, 2 M NaCl. Purified Fabs were dialyzed overnight against 20 mM Hepes pH 7.5, 150 mM NaCl. The quality of purified Fabs was analyzed by sodium dodecyl sulfate–polyacrylamide gel electrophoresis.

Binding Kinetics by SPR. All SPR experiments were performed at 20 °C using a MASS-1 (Bruker) instrument. A total of 20 nM TC-Nb4, BtuF-Nb9_4, Lyso-Nb_4, and RNAs-Nb_4 were immobilized onto a NTA sensor chip via their His-tags. Twofold serial dilutions of Fab19 and Fab14 were injected following ligand immobilization on the sensor chip. For each kinetic experiment, at least five dilutions of the Fabs were tested. The kinetic parameters were determined by fitting the data using a 1:1 Langmuir model.

Expression and Purification of VcNorM and ScaDMT. VcNorM and ScaDMT were expressed in *E. coli* and purified in DDM as outlined in *SI Appendix*.

Nb Generation against VcNorM. Nbs against VcNorM were generated as described in *SI Appendix*. VcNorM was incorporated into liposomes consisting of a 3: 1 (wt/wt) mixture of *E. coli* polar lipid extract and L-α-phosphatidylcholine as described previously (55). A llama (*Llama glama*) was injected six times with liposome-reconstituted VcNorM. Peripheral blood lymphocytes were isolated from samples collected 3 to 4 d after the last immunization, and Nbs were generated as described previously (41).

NabFab Complex Formation and EM Sample Preparation. All steps were performed at 4 °C or on ice. Complex formation for VcNorM was achieved by mixing 14 μM VcNorM, 7 μM NorM-Nb17_4, 7.7 μM NabFab, and 11.2 μM anti-Fab Nb with subsequent incubation overnight with gentle agitation. Complex formation for ScaDMT was achieved by mixing 4.5 μM ScaDMT, 4.95 μM DMT-Nb16_4, 5.4 μM NabFab, and 6.75 μM Anti-Fab Nb. The complexes were concentrated using a centrifugal filter (100 kDa cutoff, Amicon) and loaded on a Superdex S200 increase column using the respective desalting buffer as a running buffer but at 0.008% DDM. Fractions containing the respective membrane proteins were collected for cryo-EM grid preparation. The final VcNorM complex sample was at a concentration of 7.1 mg/mL and was supplemented with 0.006% cholesteryl hemisuccinate. The final ScaDMT complex sample was at a concentration of 6.4 mg/mL and was not further supplemented.

Quantifoil holey carbon grids, Cu, R 1.2/1.3, 300 mesh, were glow discharged for 45 s, 25 mA using a PELCO easiGLOW glow discharger. The sample (2.0 μl) was applied to the cryo-EM grids and blotted for 2.5 to 3.5 s before plunge freezing in a liquid ethane–propane mixture with a Vitrobot Mark IV (Thermo Fisher Scientific) operated at 4 °C and 100% humidity.

EM Data Collection. Data were recorded on a Titan Krios electron microscope (Thermo Fischer Scientific) operated at 300 kV, equipped with a Gatan BioQuantum 1967 filter with a slit width of 20 eV and a Gatan K3 camera. Movies were collected semiautomatically using Thermo Fisher Scientific EPU 2 software (56) at a nominal magnification of 130,000 and a pixel size of 0.335 Å (VcNorM) and 0.33 Å (ScaDMT) per pixel in super-resolution mode. The defocus range was −0.6 to −2.8 μm. Each movie contained 40 images per stack with a dose per frame of 1.3 electrons/Å^2.

EM Data Processing, Model Building, and Refinement. For the test structure of the VcNorM complex, an initial data set of 380 movies was collected and corrected for beam-induced motion using MotionCor2 (57). A total of 139,608 particles were auto-picked in Laplacian of Gaussian (LOG) mode and extracted with threefold binning at 2.01 Å/pixel. After two rounds of 2D classification, 10,193 particles were clearly attributed to the VcNorM complex, and an initial model was calculated thereof. After one subsequent round of 3D classification, 8,514 particles were selected and refined to 12.6 Å resolution.

For the high-resolution structure of the VcNorM-containing complex, 13,009 movies were collected and corrected for beam-induced motion using MotionCor2 (57). A total of 9,711 micrographs were selected for further processing in RELION 3.1 (43). The contrast transfer function (CTF) was estimated using Gctf (58). In a combined approach of LOG-based and 2D class reference-based particle picking, a total of 6,365,855 particles were auto-picked and were sorted by 2D and 3D classification. A total of 483,559 particles were re-extracted to 0.66 Å/pixel and were subjected to another round of 3D classification. Therefrom, 433,559 particles were selected and subjected to particle polishing and per particle CTF refinement. The particles were refined to 3.68 Å resolution. Moving the fulcrum from the transmembrane domain of VcNorM into the chimeric Nb improved the overall resolution to 3.47 Å. Local resolution estimates were generated in RELION 3.1 (43).

For the test structure of the ScaDMT complex, an initial data set of 625 micrographs was collected and corrected for beam-induced motion using MotionCor2 (57). A total of 106,551 particles were auto-picked (LOG) and extracted with threefold binning at 1.98 Å/pixel. After one round of 2D classification, a class containing 3,659 particles was clearly attributed to the protein complex of interest, and an initial model was calculated thereof. After one subsequent round of 3D classification with 20,494 particles included, 10,851 particles were selected and refined to 12.3 Å resolution.

For the high-resolution structure of the ScaDMT complex, 21,251 movies were collected and corrected for beam-induced motion using MotionCor2 (57). A total of 17,957 micrographs were selected for further processing in RELION 3.1 (43). The CTF was estimated using Gctf (58). A total of 2,416,345 particles were auto-picked (LOG) and were extracted at 2.64 Å/pixel. After sorting of the particles by 2D and 3D classification, 404,841 particles were re-extracted at 0.66 Å/pixel and were subjected to particle polishing and per-particle CTF refinement. The particles were refined to 3.99 Å resolution. After one round of heterogeneous refinement in cryoSPARC v3.2 (49), 314,541 particles were selected and refined to 3.78 Å resolution by nonuniform refinement (59) with optimized per-particle defocus and optimized CTF per-group parameters. For comparability, local resolution estimates were calculated in RELION 3.1 (43).

The structure of the dimeric complex of ScaDMT was determined based on a subclass of 40,512 particles that appeared during a 3D classification of the ScaDMT complex. After one subsequent round of 3D classification, 34,100 particles were selected and refined to 8.45 Å resolution.

Model building was performed in Coot (60), and models were refined in PHENIX (61). The structure of VcNorM was built de novo. The structures of the other components were built based on rigid body docking of the crystal structures of TC-Nb4 (33) and the Fab–anti-Fab Nb complex (32). The structure of the ScaDMT:Nb complex was built based on the published crystal structure thereof (PDB ID 4WGV) (38) and the Fab–anti-Fab Nb complex (32). Due to lower map quality in the respective regions, the part of the crystal structure containing the constant part of the Fab and the anti-Fab Nb was rigid body docked into the map after the last round of refinement. For the structure of the homodimeric ScaDMT complex, the structure of the monomeric complex was docked into the map in University of California, San Francisco (UCSF) Chimera (62) and was not further refined.

X-Ray Structure Determination of the Lyso-Nb_4:NabFab Complex. Crystallization and structure determination were performed as outlined in *SI Appendix*.

In Silico Analysis of Membrane Protein–Nb Complexes. The RCSB PDB was searched for entries containing small membrane protein–Nb complexes. Using the keyword "nanobody," 618 hits were obtained. Those were inspected manually for entries containing integral membrane protein with a molecular mass <100 kDa (excluding the Nb). For each unique Nb, one membrane protein structure was analyzed. Engineered versions of the same Nb or entries where the same Nb bound to a different target protein were not taken into consideration. This resulted in 31 unique entries for in silico analysis. Subsequently, using PyMol (53), the structure of the Nb in those complexes was superimposed onto the structure of NorM-Nb17_4, which is part of the complex structure VcNorM:NorM-Nb17_4:NabFab:anti-Fab Nb (Fig. 2 *A*–*D*). Subsequently, the structures were analyzed for clashes of NabFab or the anti-Fab Nb with either the Nb target protein or with the lipid bilayer/micelle. Clashes were categorized as follows: 1) No clash, 2) overlap involving loops; these clashes describe a slight overlap of potentially flexible loops with either loops or with a secondary structure element. Whether such a clash would abolish Fab binding is unclear and may depend on the flexibility of the involved loops. 3) Overlapping secondary structure elements: these clashes include direct overlaps of secondary structure elements, which would likely interfere with NabFab binding or require significant conformational changes in the target protein. 4) Clash with micelle: these clashes describe the insertion of the NabFab and or the anti-Fab Nb into the lipid bilayer/micelle. Whether such a clash would abolish NabFab binding is unclear.

Figure Preparation and Data Analysis. Figures of structural representations were prepared in PyMol (53), UCSF Chimera (62), and UCSF ChimeraX (63). Graphs were prepared in GraphPad Prism 9. Protein sequence alignments were generated by Clustal Omega (52) and were depicted using QIAGEN CLC Genomics Workbench 12.

Data Availability. Atomic coordinates of the complexes ScaDMT:DMT-Nb16_4:NabFab:Anti-Fab Nb and VcNorM:NorM-Nb17_4:NabFab:Anti-Fab Nb models were deposited in the RCSB PDB under accession number 7PIJ for the ScaDMT complex monomer, 7PHQ for the ScaDMT complex dimer, and 7PHP for the VcNorM complex. The 3D cryo-EM maps were deposited in the Electron Microscopy Data Bank under accession numbers EMD-13438 for the ScaDMT monomer, EMD-13426 for the ScaDMT dimer, and EMD-13425 (Map1, fulcrum in micelle) and EMD-13424 (Map2, fulcrum in NorM-Nb17_4) for VcNorM. The crystal structure of the Lyso-Nb_4:NabFab complex was deposited in the PDB under accession number 7RTH. All other study data are included in the article and/or *SI Appendix*.

ACKNOWLEDGMENTS. This research was supported by Swiss National Science Foundation Grant 310030_189111 to K.P.L. and NIH Grant GM117372 to A.A.K.

Cryo-EM data were collected at the ScopeM facility at ETH Zürich, and we thank the staff of ScopeM for technical support. We thank R. Dutzler for providing the expression plasmid and purification protocols for ScaDMT, M. Mikolin for technical support with protein expression and purification, R.N. Irobalieva for help with EM data collection, and J.R. Horn for helpful discussions. X-ray diffraction data were collected at the Northeastern Collaborative Access Team beamline sector 24-ID-E (P30 GM124165) with an Eiger 16M detector (S10OD021527) at the Advanced Photon Source (DE-AC02-06CH11357).

1. K. Basu, E. M. Green, Y. Cheng, C. S. Craik, Why recombinant antibodies - benefits and applications. *Curr. Opin. Biotechnol.* **60**, 153–158 (2019).
2. G. Chen, S. S. Sidhu, J. Nilvebrant, Synthetic antibodies in infectious disease. *Adv. Exp. Med. Biol.* **1053**, 79–98 (2017).
3. J. J. Adams, S. S. Sidhu, Synthetic antibody technologies. *Curr. Opin. Struct. Biol.* **24**, 1–9 (2014).
4. S. S. Sidhu, A. A. Kossiakoff, Exploring and designing protein function with restricted diversity. *Curr. Opin. Chem. Biol.* **11**, 347–354 (2007).
5. S. Muyldermans, Nanobodies: Natural single-domain antibodies. *Annu. Rev. Biochem.* **82**, 775–797 (2013).
6. T. De Meyer, S. Muyldermans, A. Depicker, Nanobody-based products as research and diagnostic tools. *Trends Biotechnol.* **32**, 263–270 (2014).
7. C. Morrison, Nanobody approval gives domain antibodies a boost. *Nat. Rev. Drug Discov.* **18**, 485–487 (2019).
8. S. Koide, Engineering of recombinant crystallization chaperones. *Curr. Opin. Struct. Biol.* **19**, 449–457 (2009).
9. Y. Yan *et al.*, Structure of an AMPK complex in an inactive, ATP-bound state. *Science* **373**, 413–419 (2021).
10. R. Nygaard, J. Kim, F. Mancia, Cryo-electron microscopy analysis of small membrane proteins. *Curr. Opin. Struct. Biol.* **64**, 26–33 (2020).
11. T. Che *et al.*, Structure of the nanobody-stabilized active state of the kappa opioid receptor. *Cell* **172**, 55–67.e15 (2018).
12. A. C. Kruse *et al.*, Activation and allosteric modulation of a muscarinic acetylcholine receptor. *Nature* **504**, 101–106 (2013).
13. S. G. F. Rasmussen *et al.*, Structure of a nanobody-stabilized active state of the β(2) adrenoceptor. *Nature* **469**, 175–180 (2011).
14. A. Shahsavar *et al.*, Structural insights into the inhibition of glycine reuptake. *Nature* **591**, 677–681 (2021).
15. Y. Wu, Z. Chen, F. J. Sigworth, C. M. Canessa, Structure and analysis of nanobody binding to the human ASIC1a ion channel. *eLife* **10**, e67115 (2021).
16. S. Wu *et al.*, Fabs enable single particle cryoEM studies of small proteins. *Structure* **20**, 582–592 (2012).
17. R. J. Cater *et al.*, Structural basis of omega-3 fatty acid transport across the blood-brain barrier. *Nature* **595**, 315–319 (2021).
18. J. S. Bloch *et al.*, Structure and mechanism of the ER-based glucosyltransferase ALG6. *Nature* **579**, 443–447 (2020).
19. L. Rougé *et al.*, Structure of CD20 in complex with the therapeutic monoclonal antibody rituximab. *Science* **367**, 1224–1230 (2020).
20. J. Kim *et al.*, Structure and drug resistance of the *Plasmodium falciparum* transporter PfCRT. *Nature* **576**, 315–320 (2019).
21. Q. Chen *et al.*, Structures of rhodopsin in complex with G-protein-coupled receptor kinase 1. *Nature* **595**, 600–605 (2021).
22. S. Mukherjee *et al.*, Synthetic antibodies against BRIL as universal fiducial marks for single-particle cryoEM structure determination of membrane proteins. *Nat. Commun.* **11**, 1598 (2020).
23. N. Tsutsumi *et al.*, Structure of human Frizzled5 by fiducial-assisted cryo-EM supports a heterodimeric mechanism of canonical Wnt signaling. *eLife* **9**, e58464 (2020).
24. P. Dutka *et al.*, Development of "plug and play" fiducial marks for structural studies of GPCR signaling complexes by single-particle cryo-EM. *Structure* **27**, 1862–1874.e7 (2019).
25. Y. Kang *et al.*, Cryo-EM structure of human rhodopsin bound to an inhibitory G protein. *Nature* **558**, 553–558 (2018).
26. Y. Koldobskaya *et al.*, A portable RNA sequence whose recognition by a synthetic antibody facilitates structural determination. *Nat. Struct. Mol. Biol.* **18**, 100–106 (2011).
27. B. C. McIlwain *et al.*, N-terminal transmembrane-helix epitope tag for x-ray crystallography and electron microscopy of small membrane proteins. *J. Mol. Biol.* **433**, 166909 (2021).
28. J. W. Kim *et al.*, Application of antihelix antibodies in protein structure determination. *Proc. Natl. Acad. Sci. U.S.A.* **116**, 17786–17791 (2019).
29. T. Uchański *et al.*, Megabodies expand the nanobody toolkit for protein structure determination by single-particle cryo-EM. *Nat. Methods* **18**, 60–68 (2021).
30. K. R. Miller *et al.*, T cell receptor-like recognition of tumor in vivo by synthetic antibody fragment. *PLoS One* **7**, e43746 (2012).
31. P. Carter *et al.*, Humanization of an anti-p185HER2 antibody for human cancer therapy. *Proc. Natl. Acad. Sci. U.S.A.* **89**, 4285–4289 (1992).
32. J. Ereño-Orbea *et al.*, Structural basis of enhanced crystallizability induced by a molecular chaperone for antibody antigen-binding fragments. *J. Mol. Biol.* **430**, 322–336 (2018).
33. J. S. Bloch, J. M. Sequeira, A. S. Ramirez, E. V. Quadros, K. P. Locher, Generation of nanobodies targeting the human, transcobalamin-mediated vitamin B12 uptake route. bioRxiv [Preprint] (2021). https://doi.org/10.1101/2021.08.16.456495 (Accessed 9 November 2021.
34. A. Alam *et al.*, Structural basis of transcobalamin recognition by human CD320 receptor. *Nat. Commun.* **7**, 12100 (2016).
35. S. A. Mireku, M. M. Sauer, R. Glockshuber, K. P. Locher, Structural basis of nanobody-mediated blocking of BtuF, the cognate substrate-binding protein of the *Escherichia coli* vitamin B12 transporter BtuCD. *Sci. Rep.* **7**, 14296 (2017).
36. H. Akiba *et al.*, Structural and thermodynamic basis for the recognition of the substrate-binding cleft on hen egg lysozyme by a single-domain antibody. *Sci. Rep.* **9**, 15481 (2019).
37. A. Koide *et al.*, Exploring the capacity of minimalist protein interfaces: Interface energetics and affinity maturation to picomolar KD of a single-domain antibody with a flat paratope. *J. Mol. Biol.* **373**, 941–953 (2007).
38. I. A. Ehrnstorfer, E. R. Geertsma, E. Pardon, J. Steyaert, R. Dutzler, Crystal structure of a SLC11 (NRAMP) transporter reveals the basis for transition-metal ion transport. *Nat. Struct. Mol. Biol.* **21**, 990–996 (2014).
39. M. Napiorkowska, *Structural Basis of Glycan Transfer by Bacterial Oligosaccharyltransferase PglB* (ETH Zurich, 2018).
40. X. He *et al.*, Structure of a cation-bound multidrug and toxic compound extrusion transporter. *Nature* **467**, 991–994 (2010).
41. E. Pardon *et al.*, A general protocol for the generation of nanobodies for structural biology. *Nat. Protoc.* **9**, 674–693 (2014).
42. L. J. Bailey *et al.*, Locking the elbow: Improved antibody fab fragments as chaperones for structure determination. *J. Mol. Biol.* **430**, 337–347 (2018).
43. S. H. Scheres, RELION: Implementation of a Bayesian approach to cryo-EM structure determination. *J. Struct. Biol.* **180**, 519–530 (2012).
44. C. McMahon *et al.*, Yeast surface display platform for rapid discovery of conformationally selective nanobodies. *Nat. Struct. Mol. Biol.* **25**, 289–296 (2018).
45. I. Zimmermann *et al.*, Synthetic single domain antibodies for the conformational trapping of membrane proteins. *eLife* **7**, e34317 (2018).
46. J. Jumper *et al.*, Highly accurate protein structure prediction with AlphaFold. *Nature* **596**, 583–589 (2021).
47. M. Baek *et al.*, Accurate prediction of protein structures and interactions using a three-track neural network. *Science* **373**, 871–876 (2021).
48. J. Dunbar, C. M. Deane, ANARCI: Antigen receptor numbering and receptor classification. *Bioinformatics* **32**, 298–300 (2016).
49. A. Punjani, J. L. Rubinstein, D. J. Fleet, M. A. Brubaker, cryoSPARC: Algorithms for rapid unsupervised cryo-EM structure determination. *Nat. Methods* **14**, 290–296 (2017).
50. M. Haffke *et al.*, Structural basis of species-selective antagonist binding to the succinate receptor. *Nature* **574**, 581–585 (2019).
51. P. Bräuer *et al.*, Structural basis for pH-dependent retrieval of ER proteins from the Golgi by the KDEL receptor. *Science* **363**, 1103–1107 (2019).
52. F. Sievers, D. G. Higgins, Clustal Omega for making accurate alignments of many protein sequences. *Protein Sci.* **27**, 135–145 (2018).
53. W. L. DeLano, *The PyMOL Molecular Graphics System* (Version 2.0, Schrödinger, LLC, New York, 2017).
54. M. Hornsby *et al.*, A high through-put platform for recombinant antibodies to folded proteins. *Mol. Cell. Proteomics* **14**, 2833–2847 (2015).
55. E. L. Borths, B. Poolman, R. N. Hvorup, K. P. Locher, D. C. Rees, In vitro functional characterization of BtuCD-F, the *Escherichia coli* ABC transporter for vitamin B12 uptake. *Biochemistry* **44**, 16301–16309 (2005).
56. R. F. Thompson, M. G. Iadanza, E. L. Hesketh, S. Rawson, N. A. Ranson, Collection, pre-processing and on-the-fly analysis of data for high-resolution, single-particle cryo-electron microscopy. *Nat. Protoc.* **14**, 100–118 (2019).
57. S. Q. Zheng *et al.*, MotionCor2: Anisotropic correction of beam-induced motion for improved cryo-electron microscopy. *Nat. Methods* **14**, 331–332 (2017).
58. K. Zhang, Gctf: Real-time CTF determination and correction. *J. Struct. Biol.* **193**, 1–12 (2016).
59. A. Punjani, H. Zhang, D. J. Fleet, Non-uniform refinement: Adaptive regularization improves single-particle cryo-EM reconstruction. *Nat. Methods* **17**, 1214–1221 (2020).
60. P. Emsley, K. Cowtan, Coot: Model-building tools for molecular graphics. *Acta Crystallogr. D Biol. Crystallogr.* **60**, 2126–2132 (2004).
61. P. D. Adams *et al.*, PHENIX: A comprehensive Python-based system for macromolecular structure solution. *Acta Crystallogr. D Biol. Crystallogr.* **66**, 213–221 (2010).
62. E. F. Pettersen *et al.*, UCSF Chimera–A visualization system for exploratory research and analysis. *J. Comput. Chem.* **25**, 1605–1612 (2004).
63. T. D. Goddard *et al.*, UCSF ChimeraX: Meeting modern challenges in visualization and analysis. *Protein Sci.* **27**, 14–25 (2018).